A first exergy analysis of a high-temperature solar Kalina cycle for CSP in northeast México

Eduardo González-Mora[a], Javier Alejandro Hernández-Magallanes[b] and Eduardo Rincón-Mejía[c]

[a] *Universidad Autónoma del Estado de México, Toluca, México, egonzalezmo@uaemex.mx, CA*
[b] *Universidad Autónoma de Nuevo León, San Nicolás de los Garza, México, javier.hernandezmg@uanl.edu.mx*
[c] *Universidad Autónoma de la Ciudad de México, CDMX, México, eduardo.rincon@uacm.edu.mx*

Abstract:

Concentrating solar power remains a cornerstone of the global transition towards sustainable energy, offering the unique advantage of large-scale thermal energy storage for dispatchable electricity generation. In such facilities, zeotropic mixture cycles, such as the Kalina cycle, provide superior thermodynamic matching between the heat source and the working fluid through a non-isothermal boiling process known as temperature glide. Implementing these configurations at high temperatures requires a precise integration of solar collectors and thermal storage units to minimise exergy destruction across varying meteorological conditions. However, the absence of holistic optimisation frameworks that simultaneously account for parasitic loads and annual transient variability has limited the deployment of these advanced cycles in specific industrial regions like Northern Mexico. Here we show that an integrated system-level approach, coupling a hybrid genetic algorithm with a gradient-based refiner, yields a maximum design-point net exergy efficiency of 49.75% and an annual capacity factor of 60.42% for a 50 MWe facility in Monterrey. This performance represents a significant advancement over previous non-optimised configurations, demonstrating that the rigorous inclusion of solar field and storage parasitic consumptions is essential for achieving a realistic and competitive thermodynamic design. By utilising 554 equivalent full cycles of storage annually, the system effectively bridges the gap between intermittent solar availability and continuous industrial power demand. These findings provide a robust methodology for the second-law assessment of complex solar-thermal integrations, establishing a technical benchmark for high-efficiency power generation in semi-arid regions. On a broader scale, the results underscore the potential of tailoring advanced thermodynamic cycles to regional climates as a viable path for decarbonising heavy industry while maximising the utility of the available solar resource.

Keywords:

Concentrated solar power; Kalina cycle; Exergy optimisation; Thermal energy storage; Annual transient simulation.

1. Introduction

Concentrated Solar Power (CSP) plays a niche but vital role in the renewable energy mix, particularly for providing dispatchable, firm power through thermal energy storage [1]. Unlike variable sources like PV and wind, CSP complements them by addressing intermittency in high-renewable grids. CSP contributes to grid stability, offering peak-shaving up to 80%, fast ramp rates (3-6%/min), and inertia absent in inverter-based renewables [2]. Thermal storage enables several hours of dispatchable output, making it ideal for seasonal balancing and enhancing resilience during extreme weather events. However, the global CSP installed capacity stands around 6.4 GW as of mid-2023, led by China at 1.14 GW and historical leaders like Spain and USA [3]. This represents under 1% of total renewables, dwarfed by solar PV exceeding 2.2 TWp and wind. Growth is accelerating in China with over 8 GW in the pipeline, driven by hybrid bases and policy support.

In high-penetration scenarios (>50% renewables), CSP reduces curtailment, supports demand response, and coordinates with thermal/wind/PV for optimal dispatch. Models show that it cuts system costs by replacing fossil peaking units and enabling long-duration storage. As grids near 100% renewables, CSP becomes essential for flexibility beyond batteries [4,5].

Globally, most operational concentrated solar power plants use parabolic trough collectors, which represent a mature and commercially proven technology deployed across diverse geographical regions [3]. These systems demonstrate high reliability when heating working fluids to temperatures around 400°C, whereas solar power

towers emerge as the superior alternative for applications requiring higher thermal gradients [1]. To date, the commercial sector remains dominated by the steam Rankine cycle, a trend that extends beyond solar energy to encompass conventional thermal power plants, nuclear facilities, and integrated combined-cycle systems [6]. Despite its ubiquity, the traditional steam Rankine cycle is governed by a fundamental thermodynamic constraint involving the isothermal phase change during the boiling process. When generating steam from a sensible heat source, the constant-temperature evaporation of water creates a significant temperature mismatch between the heat source and the working fluid. This discrepancy, rooted in the inherent thermohydraulic properties of water, results in substantial exergy destruction within the steam generator, acting as a primary driver of cycle inefficiency and limiting the overall second-law efficiency. While alternative configurations such as the organic Rankine cycle are frequently proposed, they typically inherit this same isothermal limitation, and although supercritical carbon dioxide cycles offer a promising path forward, their application is largely restricted to the high-temperature regimes of central receiver solar towers [7].

The Kalina cycle represents a compelling departure from pure-fluid cycles, particularly for low-to-medium temperature applications including geothermal energy, waste heat recovery, and solar thermal systems [8]. It employs a zeotropic ammonia-water mixture as the working fluid to enhance thermal efficiency through superior heat transfer matching. Operating with ammonia concentrations typically ranging from 50% to 90%, the cycle undergoes phase changes in several critical stages, beginning with a heat exchanger that absorbs energy from the source to vaporise an ammonia-rich solution [9]. This vaporous mixture subsequently expands through a turbine, followed using separators to divide the rich and lean solutions while condensers and recuperators recover latent heat during the rejection phase. Unlike pure water, which evaporates at a constant temperature, zeotropic mixtures exhibit a phenomenon known as temperature glide, which refers to the gradual change in temperature during phase transitions. This glide allows the working fluid's temperature profile to more closely follow that of the heat source or sink, thereby minimising exergy losses caused by temperature pinches and boosting second-law efficiency by 10% to 20% compared to equivalent Rankine cycles [10,11]. Furthermore, this characteristic enhances system flexibility across varying temperature ranges without necessitating excessive superheating or subcooling, thereby reducing irreversibilities in the heat exchangers.

Research has produced several specialised Kalina cycle system configurations tailored to specific industrial requirements, such as the KCS1, which is a basic setup for high-temperature sources above 400°C and achieves approximately 25% efficiency. For lower temperature regimes between 80°C and 150°C, the KCS11 incorporates recuperative heat exchangers for cogeneration or waste heat recovery, while the KCS34 is optimised for industrial exhaust in the 120°C to 200°C range, utilising low-temperature recuperators to boost power output. Building upon these foundations, the KCS234, or K234, targets the medium-temperature range of 300°C to 450°C by combining elements of previous architectures with dual separators and staged expansion to improve exergy efficiency by 5% to 10% relative to standard configurations [12]. Comparative analyses indicate that integrating these cycles with parabolic troughs results in a 5% to 20% performance increase over organic Rankine cycles due to superior glide matching [13].

In the specific context of Mexico, there exists significant solar exergy potential concentrated within the northern regions of the country [14]. Current concentrated solar power infrastructure includes the Agua Prieta Integrated Solar Combined Cycle facility, which incorporates a 14 MW parabolic trough booster [15], alongside plans for a 50 MW solar tower. While previous Mexican scholarship has explored direct steam generation Rankine cycles and conducted a singular Kalina cycle analysis for the Agua Prieta site [16], a notable research gap remains regarding the thermodynamic assessment of high-temperature Kalina cycles in other strategic locations. Monterrey, a prominent industrial hub, presents a compelling case for such a study due to its distinct meteorological conditions and substantial industrial energy demand. Boasting an annual solar irradiance of 2012.76 kWh/m^2 and exceeding 4000 hours of insolation, the city represents a highly suitable environment for the implementation of advanced concentrated solar power technologies. The primary objective of this work is to perform a comprehensive first law and second law (exergy) analysis of a 50 MWe parabolic trough-driven K234 plant equipped with seven hours of thermal energy storage, specifically tailored to the Monterrey climate. This research introduces several novel contributions to the field, beginning with the integration of power block optimisation using the PIKAIA genetic algorithm alongside system sizing for a Mexican site beyond the established Agua Prieta baseline. Furthermore, the study employs an annual transient simulation that establishes a critical link between meteorological variability and exergy performance over a full operating year. Finally, this work establishes a foundational model intended for future advanced exergy analyses, which will involve the decomposition of irreversibilities into endogenous, exogenous, avoidable, and unavoidable components.

2. Methodology

2.1. Overview of the proposed plant

The proposed facility is situated in Monterrey, Nuevo León, a strategic location characterised by substantial industrial energy demand and an exceptional solar resource. This region experiences over 4000 hours of

insolation annually, with direct irradiance exceeding 2 MWh/m^2, providing a robust foundation for the implementation of concentrated solar power technologies. The plant architecture integrates three primary subsystems: a solar collector field, a thermal energy storage unit, and a high-temperature K234 Kalina power block, as depicted in Figure 1. The solar field utilises Therminol VP-1 as the heat transfer fluid and comprises of Abengoa ASTR0 parabolic trough collectors [17], which are specifically engineered for high-efficiency thermal energy collection in utility-scale applications.

To ensure operational dispatchability and mitigate the effects of solar intermittency, the system incorporates a two-tank indirect thermal energy storage configuration utilising molten salts as the storage medium. This subsystem is sized to provide seven hours of storage at nominal load, allowing extended power generation beyond daylight hours. The power block employs the K234 Kalina cycle configuration, which is uniquely suited to match the temperature profiles generated by the parabolic trough solar field, thereby enhancing overall thermodynamic performance. The facility is designed to achieve a net electrical capacity of 50 MWe, a figure that accounts for the parasitic power consumption of the primary pumping systems within both the power block and the thermal energy storage circuit. This integrated approach ensures that the performance assessments reflect the actual net energy delivered to the grid under realistic operating conditions.

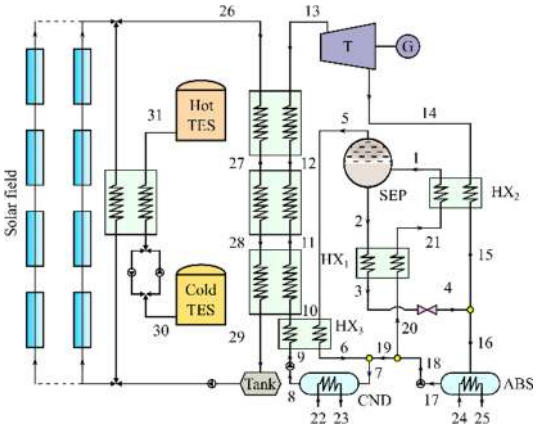

Figure. 1. *Schematic of the solar K234 cyle.*

2.2. Power block: KCS 234 configuration and optimization

The configuration of the K234 power block is illustrated in Figure 1, depicting a complex arrangement designed to maximise thermal matching. Unlike conventional Rankine cycles that rely on turbine bleed steam for feed-water heating, the K234 achieves internal heat recovery through a network of three recuperative heat exchangers, maintaining a continuous expansion process without steam extractions. The cycle architecture comprises a vapour generator (Heat Recovery Steam Generator, HRSG) coupled to the solar field, a high-pressure turbine (T), a condenser (CND), an absorber (ABS), a separator (SEP), and several auxiliary components including throttle valves, two circulating pumps, two mixers, and a splitter. This arrangement allows the system to operate across three distinct pressure levels, thereby optimizing the phase-change characteristics of the ammonia-water mixture.

The performance of the power block is highly dependent on the composition of the working fluid. In this study, the ammonia-water mixture is defined by a weak solution concentration of 0.4, while the rich-vapour concentration at the separator outlet reaches 0.97. The turbine inlet conditions are fixed at 380 ºC and 100 bar. To facilitate the thermodynamic modelling, several governing assumptions are established for the design-point analysis, which corresponds to solar noon on the summer solstice (21 June) in Monterrey. The system is modelled under steady-state conditions, with pressure drops neglected across the heat exchangers and piping to isolate the fundamental thermodynamic performance. The isentropic efficiencies are set at 0.85 for the turbine and 0.75 for the cycle pumps, while the secondary pumping systems for the thermal energy storage system and the solar field are assigned efficiencies of 0.7 and 0.8, respectively.

Thermal constraints are strictly observed to ensure physical feasibility, with a minimum approach temperature (pinch point) of 8°C maintained in the primary heat exchangers and 4°C in the condenser and absorber. For the second law (exergy) analysis, the reference environmental state is defined by the specific local ambient conditions of Monterrey, recorded as 34.7°C and 0.961 bar [18]. These parameters provide the baseline for calculating exergy destruction across each component and evaluating the overall second-law efficiency of the integrated plant.

2.3. Solar field subsystem

The solar field subsystem is designed based on reference conditions at solar noon, defined by a direct normal irradiance (G_{bn}) of 890 W/m^2 and ambient parameters of 34.7 ºC and 0.961 bar. The technology employed is the ASTRO parabolic trough collector [17], which features an aperture width of 5.77 m and modules approximately 12 m in length. Each collector utilises a standard evacuated receiver tube with an external diameter of 70 mm and an internal diameter of 65 mm [19]. Therminol VP1 is selected as the heat transfer fluid (HTF) due to its status as the industry standard for such systems and its operational range that aligns with the peak temperatures required by the K234 power block, reaching approximately 380 ºC at the turbine inlet. The solar field layout consists of modules connected in series and parallel loops to satisfy the thermal requirements of the power cycle. Each loop is constrained to a length of less than 1 km to prevent excessive parasitic pumping power, while the flow rate is managed to ensure that the HTF remains in a turbulent regime to facilitate optimal heat transfer [20].

The optical and thermal modelling of the collectors considers a selective receiver tube with an absorptance (α) of 0.96 and an emittance (ε) of 0.1, protected by a glass cover with a transmittance (τ) of 0.97. The collectors themselves possess a reflectance (ρ) of 0.93, and the model incorporates an interception factor (Γ) of 0.92 alongside a clean-soiling factor ($F_{\mathrm{c-sf}}$) of 0.92. While the peak optical efficiency is defined by the product of these intrinsic properties, the system's performance under varying solar positions is determined by an Incidence Angle Modifier (IAM) derived from ray-tracing analysis specific to the ASTRO geometry. Thermal losses from the receiver are characterised through a polynomial correlation, Eq. (1), obtained by solving the thermohydraulic model described by González-Mora et al. [21], which is integrated into the governing equations for useful heat gain. This energy balance, Eq. (2), accounts for G_{bn}, the collector aperture area (A_{col}), the angle of incidence (θ_{i}), peak optical efficiency η_{o}, the IAM, and the soiling factor to determine the temperature increment across each module.

$$\dot{q}'_{\mathrm{loss}} = (86.126 - 0.114\Delta T + 0.001\Delta T^2) \frac{\left(1-G_{\mathrm{bn_{des}}}\right)}{1\left[\frac{\mathrm{kW}}{\mathrm{m^2}}\right]}(77.75 + 0.006\Delta T + 0.00002\Delta T^2) \quad (1)$$

$$\dot{Q}_{\mathrm{gain,HTF}} = A_{\mathrm{col}} G_{\mathrm{bn}} \cos\theta_{\mathrm{i}}\, \eta_{\mathrm{o}} IAM F_{\mathrm{c-sf}} - \dot{q}'_{\mathrm{loss}} L_{\mathrm{col}} = \dot{m}_{\mathrm{HTF}} c_{\mathrm{HTF}} \Delta T_{\mathrm{HTF}} \quad (2)$$

To ensure a total temperature rise of 100 ºC across the solar field, the HTF is designed to enter at 295 ºC and exit at 395 ºC. The solar field must be significantly oversized to accommodate the integration of thermal energy storage, a requirement defined by the solar multiple, as shown in Eq. (3). For the Monterrey site, which provides approximately 12 hours of effective insolation ($G_{\mathrm{bn}} > 300$ W/m^2) on the design day, the solar field is dimensioned to support seven hours of discharge capacity. Finally, the pumping power requirements, which are essential for the subsequent system optimisation, are calculated based on the pressure drop across the loops using the Colebrook-White relationship to account for the frictional losses within the piping network.

$$SM = \frac{\dot{Q}_{\mathrm{SF}}}{\dot{Q}_{\mathrm{in,PB}}} = 1 + \frac{T_{\mathrm{disch}}}{T_{\mathrm{char}}\eta_{\mathrm{TES}}} \quad (3)$$

2.4. Thermal energy storage subsystem

The thermal energy storage (TES) subsystem employs a two-tank indirect configuration utilising "solar salt"—a eutectic mixture of 60% $NaNO_3$ and 40% KNO_3—as the storage medium. This salt is a well-established choice in the concentrated solar power industry, particularly for parabolic trough applications, due to its stable thermophysical properties [2]. In this arrangement, the cold and hot tanks are maintained at 280°C and 385°C, respectively. These operating temperatures effectively mitigate the risk of solidification, as the mixture remains well above its freezing point of 220°C, thereby ensuring the reliability of the storage cycle. Given that the solar multiple is greater than unity, the system is designed to store excess thermal energy during periods of high insolation for later use.

The operational logic for charging and discharging the system is governed by the instantaneous thermal equilibrium between the solar field's output and the power block's requirements. When the solar field is unable to meet the thermal demand of the K234 cycle, molten salt from the hot tank is circulated through a heat exchanger to heat the Therminol VP1, with the resulting lower-energy salt then stored in the cold tank, Eq. (4). Conversely, when the solar field generates more thermal energy than is required by the power block, this surplus is redirected to the storage system, Eq. (5). Heat transfer between the heat transfer fluid and the molten salt is facilitated by a shell-and-tube heat exchanger, the performance of which is evaluated using González-Mora's [22] definition, establishing efficiency as a function of heat exchanger effectiveness (ε) and the Number of Transfer Units (NTU) (Eq. 6).

$$\dot{Q}_{\mathrm{TES,dis}} = \dot{Q}_{\mathrm{in,PB}} - \dot{Q}_{\mathrm{SF}} \quad (4)$$

$$\dot{Q}_{\mathrm{TES,sto}} = \dot{Q}_{\mathrm{SF}}\dot{Q}_{\mathrm{in,PB}} \quad (5)$$

$$\eta_{\mathrm{HX}} = \frac{1}{NTU}\frac{1}{\frac{1}{\varepsilon}-\frac{1+C_{\mathrm{r}}}{2}} \quad (6)$$

Regarding parasitic energy consumption, the transport of the molten salt is managed by independent pumps, as the storage tanks are not pressurised. While the hydraulic head in such facilities typically varies between 10 and 20 bar, a design head of 15 bar is assumed for the purpose of this study. Finally, the physical volume of the storage tanks is calculated based on the total thermal energy required to sustain the power block at its nominal capacity (Q_{TES}) for the designated seven-hour storage duration, accounting for the specific energy density (E_{TES}) of the solar salt at the defined temperature gradient, as follows:

$$V_{\mathrm{TES}} = \frac{Q_{\mathrm{TES}}}{E_{\mathrm{TES}}} \quad (7)$$

2.5. Integrated thermodynamic model of the complete system

The integration of the subsystems is achieved through a primary HTF loop that facilitates energy exchange between the solar field, the thermal energy storage unit, and the HRSG of the K234 power block. From an energetic perspective, the coupling is governed by the energy balance at the HSG, where the thermal energy supplied by the HTF is assumed to be equivalent to the heat absorbed by the ammonia-water working fluid Eq. (8). Furthermore, the operational continuity of the plant is defined by the mass and energy balances corresponding to the charging and discharging modes of the storage system. To determine the actual energy delivered to the grid, the net power output ($\dot{W}_{\mathrm{net}}$) is defined as the gross turbine power ($\dot{W}_{\mathrm{t}}$) minus the cumulative parasitic consumption from the solar field pumps ($\dot{W}_{\mathrm{p,SF}}$), the thermal energy storage pumps ($\dot{W}_{\mathrm{p,TES}}$), and the internal circulating pumps for the condenser ($\dot{W}_{\mathrm{p,cnd}}$) and absorber ($\dot{W}_{\mathrm{p,abs}}$), as in Eq. (9). The entire facility is dimensioned to maintain a nominal net capacity of 50 MWe based on this energy balance.

$$\dot{Q}_{\mathrm{HRSG}} = \dot{m}_{\mathrm{VP1}}c_{\mathrm{VP1}}\Delta T_{VP1} = \dot{m}_{\mathrm{NH_3H_2O}}\Delta h_{\mathrm{NH_3H_2O}} \quad (8)$$

$$\dot{W}_{\mathrm{net}} = \dot{W}_{\mathrm{t}} - \dot{W}_{\mathrm{p,SF}} - \dot{W}_{\mathrm{p,TES}} - \dot{W}_{\mathrm{p,cnd}} - \dot{W}_{\mathrm{p,abs}} \quad (9)$$

Following the characterisation, a comprehensive exergy analysis is implemented to identify the location and magnitude of thermodynamic irreversibilities. For the solar collectors, the model evaluates the exergy change of the HTF in streams 29 and 26, as well as the exergy of the incident solar radiation following the González-Mora et al. [23] formulation, Eq. (10) and Eq. (11). For the storage tanks and heat exchangers, the analysis relies on the exergy change of the charging/discharging process between streams 30 and 31. Within the power block, the exergy of each ammonia-water stream, Eq. (12), is calculated by summing its physical exergy, Eq. (13), and its chemical exergy, Eq. (14). The inclusion of the chemical component is fundamental due to the volatile nature of the zeotropic mixture and the varying concentrations present across the cycle's state points. To define the chemical exergy, this study follows the methodology developed in [24–26]. This approach accounts for the fact that the mixture reaches thermal equilibrium with the environment while maintaining mechanical and chemical gradients.

$$\eta_{\mathrm{sun}} = \left[1 - \frac{1}{\xi_{\mathrm{sun}}}\left(\frac{T_{\mathrm{a}}}{T_{\mathrm{sun}}}\right)^4\right]\left(1 - \frac{\lambda_{\mathrm{i}}T_0}{\lambda_{\mathrm{i}}T_{\mathrm{a}}+\sigma\left(\xi_{\mathrm{sun}}T_{\mathrm{sun}}^4 - T_{\mathrm{a}}^4\right)}\right) \quad (10)$$

$$4\sigma^2 T_{\mathrm{a}}^{11} - 8\sigma\lambda_{\mathrm{i}}T_{\mathrm{a}}^8 - 8\sigma^2\xi_{\mathrm{sun}}T_{\mathrm{sun}}^4 T_{\mathrm{a}}^7 + 4\lambda_{\mathrm{i}}^2 T_{\mathrm{a}}^5$$

$$-T_{\mathrm{a}}^4(3T_0\lambda_{\mathrm{i}}^2 - 8\lambda_{\mathrm{i}}\sigma\xi_{\mathrm{sun}}T_{\mathrm{sun}}^4 + 4\,T_{\mathrm{a}}^3\sigma^2\,\xi_{\mathrm{sun}}^2 T_{\mathrm{sun}}^8 - \lambda_{\mathrm{i}}^2 T_0\xi_{\mathrm{sun}}T_{\mathrm{sun}}^4 = 0 \quad (11)$$

$$ex_{\mathrm{i}} = ex_{\mathrm{i}}^{\mathrm{ph}} + ex_{\mathrm{i}}^{\mathrm{ch}} \quad (12)$$

$$ex_{\mathrm{i}}^{\mathrm{ph}} = (h - h_0) - T_0(s - s_0) \quad (13)$$

$$ex_{\mathrm{i}}^{\mathrm{ch}} = x_{\mathrm{i}}ex_{\mathrm{NH_3}}^{\mathrm{ch}} + (1 - x_{\mathrm{i}})ex_{\mathrm{H_2O}}^{\mathrm{ch}} + w_{\mathrm{mix}} \quad (14)$$

$$w_{\mathrm{mix}} = \left(h_{\mathrm{i},0} - x_{\mathrm{i}}h_{\mathrm{NH_3},0} - (1 - x_{\mathrm{i}})h_{\mathrm{H_2O},0}\right) - T_0\left(s_{\mathrm{i},0} - x_{\mathrm{i}}s_{\mathrm{NH_3},0} - (1 - x_{\mathrm{i}})s_{\mathrm{H_2O},0}\right) \quad (15)$$

The overall performance is established through instantaneous efficiency metrics for both energy and exergy. The instantaneous energy efficiency of the solar field is calculated as the ratio of the power delivered by the collectors and the storage discharge to the sum of the incident solar radiation and the available discharge power, Eq. (16). Similarly, the thermal efficiency of the K234 cycle is defined as the ratio of net mechanical power to the required thermal input, as shown in Eq. (17). The total instantaneous energy efficiency of the plant is then the product of these two subsystems, Eq. (18). This structure is mirrored for the second-law

analysis: the instantaneous exergy efficiency of the solar field, Eq. (19), and the power block, Eq. (20), are evaluated using exergy-based equivalents of the aforementioned power and heat terms. Finally, the total instantaneous exergy efficiency is determined as the product of the individual exergy efficiencies of the solar-storage subsystem and the power block, Eq. (21).

$$\eta_{\mathrm{I,SF}} = \frac{\dot{m}_{\mathrm{VP1}}(h_{26}-h_{29})+\dot{m}_{\mathrm{TES}}(h_{31}-h_{30})}{A_{\mathrm{SF}}G_{\mathrm{bn}}+\dot{Q}_{\mathrm{TES,av}}} \quad (16)$$

$$\eta_{\mathrm{II,SF}} = \frac{\dot{m}_{\mathrm{VP1}}(ex_{26}-ex_{29})+\dot{m}_{\mathrm{TES}}(ex_{31}-ex_{30})}{A_{\mathrm{SF}}G_{\mathrm{bn}}\eta_{\mathrm{sun}}+\dot{E}x_{\mathrm{TES,av}}} \quad (17)$$

$$\eta_{\mathrm{I,PB}} = \frac{\dot{W}_{\mathrm{net}}}{\dot{Q}_{\mathrm{in}}} \quad (18)$$

$$\eta_{\mathrm{I,PB}} = \frac{\dot{W}_{\mathrm{net}}}{\dot{E}x_{\dot{Q}_{\mathrm{in}}}} \quad (19)$$

$$\eta_{\mathrm{I,tot}} = \eta_{\mathrm{I,SF}}\eta_{\mathrm{I,PB}} \quad (20)$$

$$\eta_{\mathrm{II,tot}} = \eta_{\mathrm{II,SF}}\eta_{\mathrm{II,PB}} \quad (21)$$

To evaluate the long-term viability of the plant beyond instantaneous design-point conditions, the methodology incorporates a series of cumulative annual performance indices. The annual average energy and exergy efficiencies are defined as the ratio of the total useful output delivered by the system over a full operating year to the total resource availability during the same period. Rather than treating these as separate phenomena, they are defined as the fraction of the cumulative annual energy (or exergy) potential that the system successfully converts into its respective useful form, as described in Eqs. (22) and (23). This approach ensures a holistic characterisation of the system's ability to manage fluctuating meteorological conditions in Monterrey while maintaining efficient energy conversion.

$$\bar{\eta}_{\mathrm{I,tot}} = \frac{\int \dot{W}\mathrm{d}t}{\int (\dot{Q}_{\mathrm{sun}}+\dot{Q}_{\mathrm{TES}})\mathrm{d}t} \quad (22)$$

$$\bar{\eta}_{\mathrm{II,tot}} = \frac{\int \dot{W}\mathrm{d}t}{\int (\dot{E}x_{sun}+\dot{E}x_{\mathrm{TES}})\mathrm{d}t} \quad (23)$$

Furthermore, two additional metrics are utilised to contextualise the plant's operational effectiveness within the Mexican industrial landscape. The first is the solar fraction (SF), which quantifies the system's thermal autonomy by defining the portion of the total annual thermal demand that is met by the energy captured and delivered by the solar field, Eq. (24). This parameter is critical for assessing the degree to which the CSP facility reduces reliance on auxiliary or conventional energy sources. The second metric is the capacity factor (CF), which relates the actual net electrical energy generated by the plant during the annual cycle to the theoretical energy output that would have been achieved had the facility operated continuously at its nominal 50 MWe capacity, Eq. (25). Together, these metrics provide a robust framework for evaluating the technical maturity and reliability of the K234-driven plant over a representative temporal horizon.

$$SF = \frac{\int \dot{Q}_{\mathrm{SF-load}}\mathrm{d}t}{\int \dot{Q}_{\mathrm{in,PB}}\mathrm{d}t} \quad (24)$$

$$CF = \frac{\int \dot{W}_{\mathrm{gen}}\mathrm{d}t}{\int \dot{W}_{\mathrm{net}}\mathrm{d}t} \quad (25)$$

2.6. Optimization methodology

The final stage of the methodology establishes a holistic optimisation framework designed to ensure the global performance of the integrated facility, rather than focusing on the isolated performance of individual subsystems. This system-level approach is necessitated by the complex thermodynamic interactions between the solar field, the thermal energy storage unit, and the power block, where an improvement in one component may inadvertently compromise the efficiency of another. Consequently, the optimisation procedure aims to maximise the net exergy efficiency of the entire plant at the design point, Eq. (21), a metric that inherently accounts for the cumulative irreversibilities and parasitic loads across all subsystems. The primary decision variables selected for this procedure include the turbine outlet pressure, the temperature of the hot stream at the outlet of the high-temperature recuperator (HX2), and the concentration of the strong ammonia-water solution at the separator inlet. While the solar field and thermal energy storage units are not direct decision variables in the optimisation loop, they are dynamically sized within each iteration to match the power block's requirements, ensuring that their associated pumping powers are accurately reflected in the objective function.

To ensure the physical and thermodynamic feasibility of the resulting configurations, the optimisation is subject to several critical constraints. Vapour quality at the turbine outlet is maintained above 0.9 to prevent blade erosion, while the quality of the strong solution at the separator inlet is required to be greater than zero to ensure proper phase separation. Furthermore, thermal constraints are strictly observed through the enforcement of minimum approach temperatures, specifically limited to 8°C in the primary heat exchangers and 4°C in the condenser and absorber units. The optimisation process is executed in two distinct phases to navigate the highly non-linear landscape of ammonia-water thermodynamic properties. Initially, the PIKAIA genetic algorithm is employed to explore the global solution space and avoid entrapment in local optima. This algorithm uses a population size of 30—equivalent to ten times the number of decision variables—and is permitted to run for 200 generations to facilitate comprehensive exploration. A mutation rate of 0.15 is initially set to maintain genetic diversity, which subsequently decays as generations progress to allow for more focused convergence.

Given that Kalina cycles involve significant non-linearities and potential local maxima stemming from varying concentrations and pressures, the global search performed by PIKAIA is followed by a fine-tuning stage utilizing the Variable Metric Method. This gradient-based approach allows for a precise refinement of the optimum point identified by the genetic algorithm, ensuring a highly accurate final solution. The convergence criteria for this integrated optimisation framework are set at a tolerance of 1.0×10^{-4}, providing a robust balance between computational efficiency and thermodynamic precision. This dual-stage methodology ensures that the resulting design for the Monterrey facility represents the most efficient configuration possible under the specified meteorological and technical constraints.

3. Results and discussion

3.1. Optimisation results

The optimisation results for the integrated system demonstrate a robust convergence behaviour facilitated by the hybrid computational strategy. The PIKAIA genetic algorithm effectively navigated the complex search space to identify the basin of attraction containing the global optimum. However, given the stochastic nature of the algorithm and the inherent decay of the mutation rate, PIKAIA alone occasionally lacks the numerical precision required to pinpoint the exact local maximum. To rectify this, the Variable Metric Method was employed as a secondary gradient-based refiner. By initiating this method from the best solution found across five independent PIKAIA runs—each conducted with unique random seeds—the system achieved a precise local optimum. While the subsequent refinement yielded a relatively modest improvement of 1% in the net exergy efficiency, this step was critical in providing the necessary confidence that a true thermodynamic optimum had been reached.

Following this optimisation procedure, the thermodynamic states for all streams across the integrated plant were determined; the comprehensive data for these state points are presented in the following Table 1. These results define the peak performance of the Monterrey plant based on the optimal values for the primary decision variables: a turbine outlet pressure of 3.262 bar, a temperature of 38.02 °C at the high-temperature recuperator (HX2) outlet, and an ammonia concentration of 0.4937 for the strong solution at the separator inlet. Under these optimised conditions, the integrated facility achieved a maximum net exergy efficiency of 49.75% at the design point.

Table 1. *Thermodynamic states for the K234 CSP plant.*

i	Fluid	T_i, (K)	P_i, (bar)	Q_i	x_i	h_i, (kJ/kg)	s_i, (kJ/kg·K)	ex_i, (kJ/kg)	$\dot{m}_i$, (kg/s)
1	NH_3H_2O	353.2	9.457	0.1634	0.4937	347.1	1.635	9764	278.6
2	NH_3H_2O	353.2	9.457	0	0.4	128	0.9948	7862	232.8
3	NH_3H_2O	311	9.457	sat.	0.4	-59.37	0.43	7848	232.8
4	NH_3H_2O	311.2	3.262	sat.	0.4	-59.37	0.4324	7847	232.8
5	NH_3H_2O	353.2	9.457	0.9947	0.97	1461	4.888	19437	45.78
6	NH_3H_2O	348	9.457	0.9816	0.97	1423	4.778	19432	45.78
7	NH_3H_2O	333.5	9.457	0.4982	0.75	712.5	2.706	14944	85.07
8	NH_3H_2O	306.3	9.457	0	0.75	-15.18	0.4147	14922	85.07
9	NH_3H_2O	308.7	100	sat.	0.75	1.747	0.4284	14935	85.07
10	NH_3H_2O	313.2	100	sat.	0.75	22.5	0.4952	14935	85.07
11	NH_3H_2O	427.2	100	0	0.75	627.9	2.131	15037	85.07
12	NH_3H_2O	501.4	100	1	0.75	1871	4.806	15457	85.07
13	NH_3H_2O	653.2	100	sat.	0.75	2381	5.691	15694	85.07

14	NH_3H_2O	369.5	3.262	0.9866	0.75	1757	5.992	14977	85.07
15	NH_3H_2O	311.2	3.262	0.5698	0.75	756.3	3.106	14865	85.07
16	NH_3H_2O	314.5	3.262	0.1436	0.4937	158.9	1.149	9725	317.9
17	NH_3H_2O	300.8	3.262	0	0.4937	-115.9	0.2588	9724	317.9
18	NH_3H_2O	300.9	9.457	NA	0.4937	-114.9	0.2596	9725	317.9
19	NH_3H_2O	300.9	9.457	NA	0.4937	-114.9	0.2596	9725	39.29
20	NH_3H_2O	300.9	9.457	NA	0.4937	-114.9	0.2596	9725	278.6
21	NH_3H_2O	335.7	9.457	NA	0.4937	41.66	0.752	9730	278.6
22	Water	296.8	5	NA	NA	99.81	0.3487	1.249	543.5
23	Water	324.1	5	NA	NA	213.7	0.7158	2.137	543.5
24	Water	296.8	5	NA	NA	99.81	0.3487	1.249	1533
25	Water	310.5	5	NA	NA	156.8	0.5364	0.4529	1533
26	VP1	668.2	7	NA	NA	NA	NA	296.9	822.7
27	VP1	646.5	7	NA	NA	NA	NA	268.9	822.7
28	VP1	593.8	7	NA	NA	NA	NA	204.2	822.7
29	VP1	568.2	7	NA	NA	NA	NA	174.8	822.7
30	Solar salt	553.2	NA	NA	NA	NA	NA	97.66	1073
31	Solar salt	658.2	NA	NA	NA	NA	NA	175.2	1073

A detailed breakdown of the power distribution reveals that the turbine produces a gross output of 53.147 MW. To determine the net capacity, several parasitic loads must be accounted for: the solar field pumps require 165.5 kW, while the thermal energy storage pumps account for 1.224 MW. Within the power block itself, the condener and absorber units consume 1.440 MW and 317.4 kW, respectively. When contrasted with a non-optimised baseline, such as the Kalina cycle configuration previously analysed for the Agua Prieta facility which attained an exergy efficiency of 37%, the current study demonstrates a substantial performance increase. This improvement highlights the critical importance of system-level optimisation in bridging the gap between theoretical cycle potential and practical, high-efficiency solar thermal applications.

3.2. Solar field and thermal energy storage requirements

The physical dimensioning of the solar field and thermal energy storage (TES) subsystems was determined by the requirements for a dispatchable 50 MWe facility in the Monterrey climate. To ensure seven hours of thermal storage at nominal load, a solar multiple (SM) of 1.71 was established. This sizing is consistent with commercial parabolic trough collector (PTC) plants, indicating that the K234-driven plant maintains a competitive land-use efficiency. The resulting solar field is configured with 349 parallel loops, each comprising 24 collector modules, yielding a total loop length of 288 m. This configuration is strategic, as it remains well within the 1 km technical limit, ensuring that pressure drops across the loops are restricted to less than 1 bar, which significantly reduces the parasitic pumping power requirements.

The total concentration area for the facility is 58 hectares, a dimension that allows the field to simultaneously satisfy the power block's thermal demand and store surplus energy during peak insolation. To accommodate this seven-hour discharge capacity, the TES subsystem requires an inventory of 22625 tonnes of solar salt stored in two non-pressurised tanks. Each tank has a volume of 12127.5 m^3, resulting in a total storage capacity of 24255 m^3. This physical infrastructure provides the necessary thermal inertia to ensure the plant can operate reliably beyond daylight hours, effectively shifting solar production to meet demand.

3.3 Integrated System Performance at Design Point

The performance of the integrated plant at the design point—fixed at solar noon on 21 June—provides a definitive baseline for its peak operational capacity. At this point, the vapour generator facilitates the heating of 84.76 kg/s of the ammonia-water mixture from 154.1°C to 380°C. This thermal demand is satisfied by the circulation of 819 kg/s of Therminol VP1, operating over a temperature gradient of 295°C and 395°C, while the storage tanks maintain the molten salt at 385°C (hot) and 280°C (cold). Under these conditions, the Kalina cycle achieves an energy efficiency of 25.01% and an exergy efficiency of 49.93%, while the solar field delivers corresponding values of 69.57% and 75.63%, respectively. The heat exchange components also show high performance; the HRSG demonstrates an energy efficiency of 97.82% (despite a lower exergy yield of 64.26% due to heat transfer gradients), and the TES heat exchanger exhibits a high effectiveness of 0.913, with energy and exergy efficiencies of 0.9865 and 0.9791.

Figure 2 presents the Grassmann diagram for the complete installation, illustrating the distribution of exergy destruction across all components. A rigorous second-law analysis identifies the solar field as the primary site of irreversibility, accounting for 68.34% of the total exergy destruction, a loss fundamentally tied to the extreme temperature gradient between the solar source and the receiver. The HRSG follows, accounting for 22.15% of the destruction; although the Kalina cycle's temperature glide significantly reduces entropy generation compared to isothermal boiling, this remains a major source of loss within the power block. The turbine contributes 4.85% to the total exergy destruction, consistent with its defined isentropic efficiency.

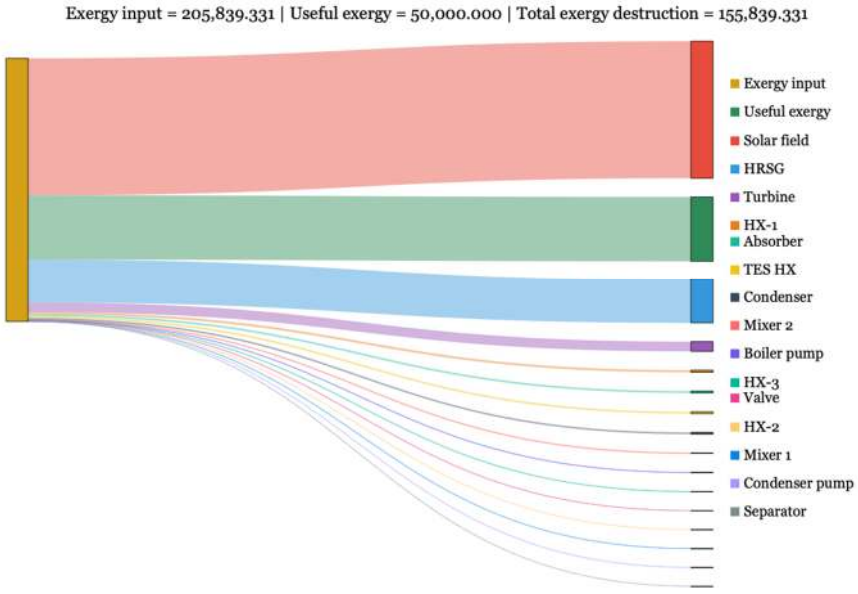

Figure. 2. *Grassmann diagram of exergy distribution.*

Remarkably, the remaining components demonstrate an exceptionally well-balanced thermal recovery network. The condenser and absorber units show destruction values of only 0.87% and 0.93%, respectively, indicating highly efficient low-temperature heat rejection. Similarly, internal recuperators such as HX1 (1.08%) and HX2 (0.07%) contribute minimally to the total loss. Finally, the separator and splitter components show 0.00% destruction, confirming that phase separation is achieved with no significant thermodynamic penalty. This breakdown confirms that after the inevitable losses in the solar field and vapour generator, the K234 cycle manages the remaining exergy with high precision, validating its integration into the Mexican solar landscape.

3.4 Annual performance results

The annual performance of the proposed facility in Monterrey was evaluated using Typical Meteorological Year (TMY) data to capture the full spectrum of local climatic variability and its impact on the integrated K234 system. The simulation yields a capacity factor of 60.42%, a robust figure that represents the ratio of actual energy generated to the theoretical maximum if the plant operated at nominal load indefinitely. For a 50 MW_e concentrated solar power (CSP) facility, this value is highly significant; while commercial plants with massive 12-hour storage arrays can reach 75%, the 60.42% achieved here with a seven-hour storage system is remarkably competitive for the Monterrey site. Over a standard operating year, the installation delivers a total of 264.65 GWh of net electricity to the grid, underscoring its potential as a reliable base-load contributor to the regional industrial sector.

A critical metric in this performance is the storage utilisation, quantified by approximately 554 equivalent full cycles (EFC) on an annual basis. In this context, the EFC represents the total energy discharged from the TES divided by the energy required to run the 50 MWe power block at full design output. Reaching 554 EFC indicates that the seven-hour storage system is being cycled effectively throughout the year, providing over 550 hours of full-load operation that would otherwise be unavailable during non-solar hours. This high cycling rate directly supports the 60.42% capacity factor by ensuring that the oversized solar field ($SM = 1.71$) does not waste surplus thermal energy, instead shifting it to meet demand during the evening or transient cloudy periods.

The operational dynamics are further illustrated in Figure 3a. The light-yellow bands represent steady 50 MW generation, where the integration of the EFC and the seven-hour TES capacity is visible as the extension of power production into the late evening hours (often until 19:00 or 20:00). The vertical dark streaks indicate Monterrey's characteristic meteorological shifts, where the TES must compensate for sudden drops in DNI.

The fact that the plant maintains nominal output during these shifts is a testament to the thermodynamic coupling between the solar field and the K234 cycle.

Regarding conversion performance, the plant achieves an average annual energy efficiency of 14.01% and a notably higher annual exergy efficiency of 19.32%. The temporal distribution of these efficiencies is captured in Figure 3b and 3c. While energy efficiency remains relatively stable around solar noon, the exergy efficiency provides a more nuanced view of the system's thermodynamic advantages. The higher exergy value (19.32%) reflects the Kalina cycle's ability to reduce heat transfer irreversibilities. Because the ammonia-water mixture boils with a temperature glide, it matches the cooling profile of Therminol VP1 more closely than a boiling Rankine fluid would. This reduced exergy destruction in the vapour generator is the primary reason the plant achieves such high second-law performance, even when subjected to the variable ambient conditions of Northern Mexico.

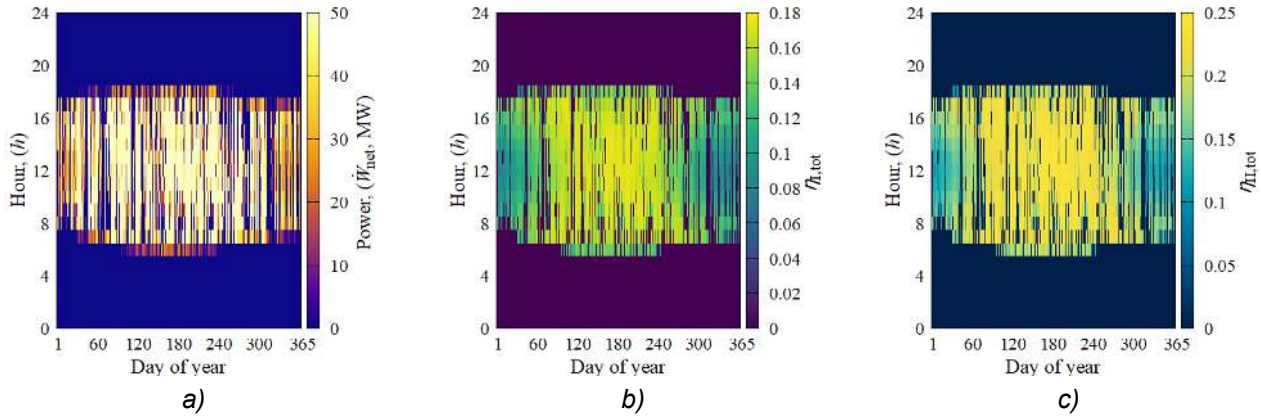

Figure. 2. *Annual performance. a) Net power output, b) Energy efficiency, c) Exergy efficiency.*

4. Conclusions

This study aimed to design and optimise an integrated high-temperature concentrated solar power (CSP) plant coupled with a K234 Kalina cycle and a two-tank molten salt storage system specifically for the climatic conditions of Monterrey, Mexico. The methodology employed a robust multi-stage approach, coupling the PIKAIA genetic algorithm for global search with the Variable Metric Method for local refinement, all integrated within an annual transient simulation framework to ensure a realistic assessment of system-wide performance.

The study reveals that the optimised plant achieves a peak net exergy efficiency of 49.75% at the design point and a capacity factor of 60.42%, delivering an annual net electrical energy of 264.65 GWh. Through the global optimisation of turbine outlet pressure, separator inlet concentration, and recuperator temperatures, the results show that the inclusion of solar field and storage parasitic loads in the objective function leads to a physically feasible design. Furthermore, the analysis identified the solar field (68.34%) and the vapour generator (22.15%) as the primary contributors to exergy destruction, highlighting the critical areas for potential thermal improvement.

However, the current assessment is limited using a simplified shell-and-tube heat exchanger model and steady-state assumptions for internal power block components, which may affect the interpretation of efficiencies during rapid meteorological transients. These constraints suggest that while the global optimum is well-defined, the precise response to sub-hourly irradiance fluctuations warrants further high-fidelity dynamic modelling to fully capture the transient behaviour of the ammonia-water mixture.

These findings significantly advance the field by providing the first integrated exergy assessment of a high-temperature solar Kalina cycle in the Mexican context, showing a marked improvement over previous non-optimised configurations which reached only 37% exergy efficiency. By coupling subsystem sizing with annual transient data and a 554 Equivalent Full Cycle storage usage, this research offers a more realistic benchmark for the dispatchability of zeotropic mixture cycles compared to standard Rankine-based CSP studies.

Future investigations should incorporate advanced exergy and exergoeconomic analyses to refine the cost-benefit ratio of the internal recovery network. Subsequent research could also explore direct molten salt parabolic trough collectors to eliminate oil-to-salt heat exchange losses or evaluate alternative zeotropic configurations and working fluids to further enhance second-law performance under varying ambient temperatures.

The present research establishes a comprehensive roadmap for the deployment of high-efficiency, dispatchable solar power plants tailored to the specific energy and climatic profiles of industrial hubs in Northern Mexico. From a wider scientific perspective, the integration of high-glide thermodynamic cycles with thermal storage represents a critical step toward transitioning global industrial infrastructure from fossil-fuel reliance to sustainable, high-exergy solar alternatives.

Acknowledgments

The authors appreciate the support provided by COMECyT through the program 'Investigadoras e Investigadores COMECyT' to EGM. This work, conducted as part of the AESCo project, was made possible by the resources and funding granted under this initiative.

Nomenclature

A aperture area, m^2

c specific heat, kJ/(kg K)

E energy density, kJ/m^3

F clean-soiling factor, (-)

G direct normal irradiance, kW/m^2

IAM Incidence Angle Modifier, (-)

$\dot{m}$ mass flow rate, kg/s

NTU number of transfer units

P pressure, bar

$\dot{q}'$ heat flux per unit length, kW/m

$\dot{Q}$ rate of thermal energy, kW

SM solar multiple, (-)

T temperature, °C

V volume, m^3

$\dot{W}$ Power, W

x mass fraction, (-)

Greek symbols

α absorptance

ε emittance

η efficiency

θ angle of incidence

ρ reflectance

τ transmittance

Subscripts and superscripts

a air

abs absorber

bn beam normal

c cleaning

ch chemical

cnd condenser

HTF heat transfer fluid

in, PB input, power block

ph physical

sf soiling factor

SF solar field

sun solar energy

TES thermal energy storage

References

[1] Lovegrove K, Stein W. Introduction to concentrating solar power technology. In: Lovegrove K, Stein W, editors. Concentrating Solar Power Technology. 2nd ed., Elsevier; 2021, p. 3–17. https://doi.org/10.1016/B978-0-12-819970-1.00012-8.

[2] Codd DS, Gil A, Manzoor MT, Tetreault-Friend M. Concentrating Solar Power (CSP)—Thermal Energy Storage (TES) Advanced Concept Development and Demonstrations. Current Sustainable/Renewable Energy Reports 2020;7:17–27. https://doi.org/10.1007/s40518-020-00146-4.

[3] Thonig R, Gilmanova A, Lilliestam J. CSP.guru 2023-07-01 2023. https://doi.org/10.5281/zenodo.8191855.

[4] Xu M, Cui Y, Wang T, Zhang Y, Guo Y, Zhang X. Optimal Dispatch of Wind Power, Photovoltaic Power, Concentrating Solar Power, and Thermal Power in Case of Uncertain Output. Energies (Basel) 2022;15:8215. https://doi.org/10.3390/en15218215.

[5] Turchetti L. Preface: SolarPACES 2024, 30th International Con-ference on Concentrating Solar Power, Thermal, and Chemical Energy Systems. SolarPACES Conference Proceedings 2025;3. https://doi.org/10.52825/solarpaces.v3i.2884.

[6] Breeze P. Power generation technologies. Newnes; 2019.

[7] Vant-Hull LL. Central tower concentrating solar power systems. In: Keith Lovegrove, Wes Stein, editors. Concentrating Solar Power Technology. 2nd ed., Elsevier; 2021, p. 267–310. https://doi.org/10.1016/B978-0-12-819970-1.00019-0.

[8] Kalina AI. Combined Cycle and Waste Heat Recovery Power Systems Based on a Novel Thermodynamic Energy Cycle Utilizing Low-Temperature Heat for Power Generation. 1983 Joint Power Generation Conference: GT Papers, American Society of Mechanical Engineers; 1983. https://doi.org/10.1115/83-JPGC-GT-3.

[9] Kalina Power. Kalina Cycle 2025. https://kalinapower.com/technology/ (accessed December 25, 2025).

[10] Ataei A, Ehyaei MA, Alizadeh MY, Ahmadi MH. Energy Analysis of Supercritical Water and Ammonia (Kalina) Power Cycle 2014.

[11] Arrieta MDP, Arrieta FRP. KCS34 evaluation for WHR in cement industry. International Journal of Advanced Engineering Research and Science 2018;5:190–6. https://doi.org/10.22161/ijaers.5.11.27.

[12] Srinivas T, Ganesh NS, Shankar R. Flexible Kalina cycle systems. Apple Academic Press; 2019.

[13] Mirjavadi K, Pourfayaz F, Pourmoghadam P, Kasaeian A. A comparison of using organic Rankine and Kalina cycles as bottom cycles in a solar-powered steam Rankine cycle. Energy Sci Eng 2022;10:2714–31. https://doi.org/10.1002/ese3.1161.

[14] Duran-Garcia MD, Gonzalez-Mora E, Lentz-Herrera A. EXERGY MAPS AS A TOOL FOR ASSESSING SOLAR ENERGY POTENTIAL IN MÉXICO. 37th International Conference on Efficiency, Cost, Optimization, Simulation and Environmental Impact of Energy Systems (ECOS 2024), Zografos, Greece: ECOS 2024; 2024, p. 2251–61. https://doi.org/10.52202/077185-0193.

[15] Abengoa. Central termosolar Agua Prieta II – 14 MW n.d. http://www.abengoa.com.mx/web/es/areas-de-actividad/ingenieria-y-construccion-industrial/energia-renovable/obra/Central-termosolar-Agua-Prieta-II-14-MW/ (accessed July 1, 2019).

[16] González-Mora E, Durán-García MaD. Assessing parabolic trough collectors and linear Fresnel reflectors direct steam generation solar power plants in Northwest México. Renew Energy 2024;228:120375. https://doi.org/10.1016/j.renene.2024.120375.

[17] ABENGOA. A new generation of parabolic trough technology. 2013.

[18] NREL. NSRDB: National Solar Radiation Database 2024. https://nsrdb.nrel.gov/data-viewer (accessed August 4, 2024).

[19] Pernpeintner J. Receivers. The Performance of Concentrated Solar Power (CSP) Systems 2017:99–112. https://doi.org/10.1016/B978-0-08-100447-0.00004-3.

[20] Zarza Moya E. Parabolic-trough concentrating solar power systems. In: Lovegrove K, Stein W, editors. Concentrating Solar Power Technology. 2nd ed., Elsevier; 2021, p. 219–66. https://doi.org/10.1016/B978-0-12-819970-1.00009-8.

[21] González-Mora E, Durán-García MD. Alternative Approach for Thermo-Hydraulic Modeling of Direct Steam Generation in Parabolic Trough Solar Collectors. J Therm Sci Eng Appl 2024;16:1–12. https://doi.org/10.1115/1.4064819.

[22] González-Mora E. A RATIONAL EFFICIENCY DEFINITION FOR HEAT EXCHANGERS. System Research in Energy 2025;2025:123–34. https://doi.org/10.15407/srenergy2025.04.123.

[23] González-Mora E, Poudel R, Durán-García MD. A practical upper-bound efficiency model for solar power plants. Journal of Non-Equilibrium Thermodynamics 2023. https://doi.org/10.1515/jnet-2022-0080.

[24] MOROSUK T, TSATSARONIS G. A new approach to the exergy analysis of absorption refrigeration machines. Energy 2008;33:890–907. https://doi.org/10.1016/j.energy.2007.09.012.

[25] Gaggioli R. The Dead State. International Journal of Thermodynamics 2012;15. https://doi.org/10.5541/ijot.423.

[26] Palacios-Lorenzo ME, Marcos JD. Downsizing strategy for an air-cooled indirect-fired single-effect ammonia-water absorption chiller in part-load operation in hot climates. Case Studies in Thermal Engineering 2024;53:103911. https://doi.org/10.1016/j.csite.2023.103911.